



Geotechnical Testing Journal

Abhishek Rawat,¹ Wiebke Baille,² Snehasis Tripathy,³ and Tom Schanz⁴

DOI: 10.1520/GTJ20180192

A Column-Type Experimental
Device for Investigating Coupled
Thermo-Hydro-Mechanical
Behavior of Expansive Soils

Abhishek Rawat,¹ Wiebke Baille,² Snehasis Tripathy,³ and Tom Schanz⁴

A Column-Type Experimental Device for Investigating Coupled Thermo-Hydro-Mechanical Behavior of Expansive Soils

Reference

A. Rawat, W. Baille, S. Tripathy, and T. Schanz, "A Column-Type Experimental Device for Investigating Coupled Thermo-Hydro-Mechanical Behavior of Expansive Soils," *Geotechnical Testing Journal* <https://doi.org/10.1520/GTJ20180192>

ABSTRACT

This paper presents a newly designed column-type experimental device for investigating the coupled thermo-hydro-mechanical behavior of expansive soils. Sensors and monitoring instruments facilitated continuous and nondestructive measurements of temperature, relative humidity, water content, and total stresses in both axial and lateral directions at various pre-selected locations of the device. The design features and calibration of specific accessories are presented. System implementation and validation tests were performed to examine the performance of the device at an elevated temperature. In the context of underground storage of nuclear waste, a test was performed with a compacted Calcigel bentonite-sand mixture (50:50) to investigate the thermo-hydro-mechanical behavior of the material under an applied temperature gradient involving temperatures of 80°C and 20°C at the opposite ends of the sample. The test results highlighted the key features of temperature-driven processes in unsaturated compacted porous media. Thermal loading caused changes in the water content and relative humidity within the sample. During the temperature equilibration period, the thermal dilation phenomenon in the regions closer to the heat source was found to be responsible for the development of axial and lateral stresses in the sample. A longer duration of thermal loading caused volumetric shrinkage of the material, which in turn affected the magnitudes of both axial and lateral stresses.

Keywords

coupled thermo-hydro-mechanical behavior, laboratory test, expansive soils, unsaturated soil, nuclear waste repository

Manuscript received September 21, 2017; accepted for publication April 26, 2021; published online July 6, 2021.

¹ Department of Civil and Environmental Engineering, Ruhr University Bochum, Universitaetsstr. 150, Bochum 44801, Germany, <https://orcid.org/0000-0001-7489-3073>

² Department of Civil and Environmental Engineering, Ruhr University Bochum, Universitaetsstr. 150, Bochum 44801, Germany (Corresponding author), email: wiebke.baille@rub.de, <https://orcid.org/0000-0001-6852-9427>

³ School of Engineering, Cardiff University, Queen's Buildings, West Grove, Newport Rd., Cardiff CF24 3AA, UK, <https://orcid.org/0000-0003-1632-7668>

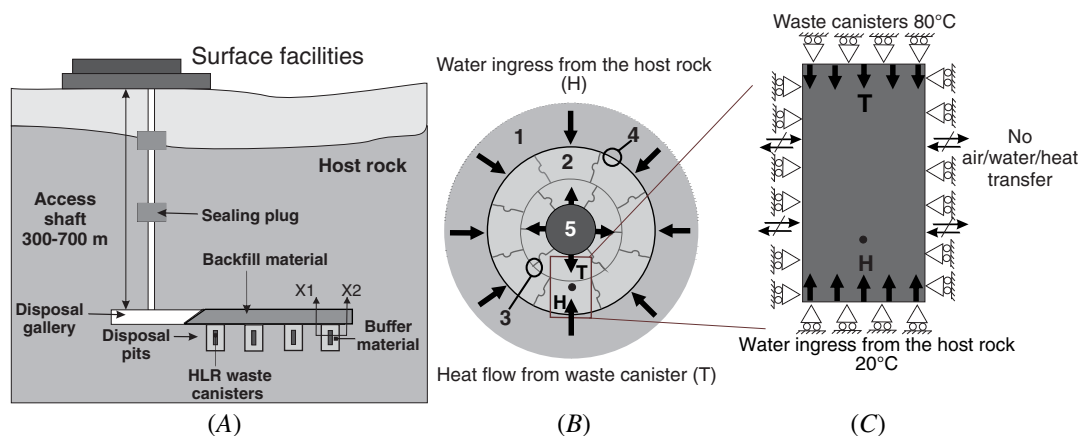
⁴ Department of Civil and Environmental Engineering, Ruhr University Bochum, Universitaetsstr. 150, Bochum 44801, Germany (deceased)

Introduction

The coupled heat and moisture flow through soils are prevalent in several geotechnical engineering applications, such as subsurface installation of high-voltage power cables, extraction of geothermal energy using boreholes, installation of compacted clay liners in waste disposal projects, and the application of bentonite-based barriers at deep geological repository for high-level radioactive waste disposal. A schematic of the deep geological repository showing the salient features is presented in [figure 1A](#). Compacted bentonites and bentonite–sand mixtures are proposed to be used as the barrier and backfilling materials in underground disposal of high-level radioactive (HLR) waste in many countries ([Pusch and Yong 2006](#)). In such applications, the thermal, hydraulic, and mechanical processes within the materials are strongly coupled and considered extremely important in numerical modeling for assessing the long-term behavior of the repositories. Determination of design parameters (e.g., stress, temperature, and gas pressure) and assessments of long-term material behavior associated with changes in water content and relative humidity (suction) require testing of the barrier and backfilling materials under the repository-relevant thermal (T), hydraulic (H), and mechanical (M) boundary conditions.

Several full-scale experiments have been conducted either in the field or in the laboratory under the coupled THM loading scenarios relevant to the deep geological disposal of high-level radioactive waste ([Alonso et al. 2005](#); [Gens et al. 2007](#)). For instance, a Full-scale Engineered Barriers Experiment (FEBEx) test was commissioned at the Grimsel underground research laboratory in Switzerland ([Alonso et al. 2005](#)). Similarly, a laboratory-based full-scale mock-up experiment was carried out as a forerunner of the FEBEx field test under controlled boundary conditions ([Martín and Barcala 2005](#)). Apart from the initial installation cost, the laboratory-based investigations have certain advantages over the field investigations and mock-up tests, such as a precise control over the applied thermal and hydraulic gradients, efficient data monitoring, and a reasonable testing period. In this regard, several small-scale experiments have been performed using a column-type testing device ([Cuevas et al. 1997](#); [Yong et al. 1997](#); [Börgesson et al. 2001](#); [Pintado, Ledesma, Lloret 2002](#); [Gatabin and Billaud 2005](#); [Villar, Martín, and Barcala 2005](#); [Åkesson et al. 2009](#); [Schanz, Nguyen-Tuan, and Datcheva 2013](#); [Saba et al. 2014](#); [Tripathy, Thomas, and Bag 2015](#)). [Figure 1B](#) depicts the sectional view of a disposal pit in deep disposal of radioactive waste that links the column-type testing concept ([fig. 1C](#)) for investigating the material behavior under the repository-relevant boundary conditions. In the column-type testing concept, the barrier and backfill materials are subjected to thermal and hydraulic loadings under the K_0 condition. The changes in temperature, relative humidity, and the

FIG. 1 (A) A schematic illustration of the deep geological disposal concept, (B) sectional view of disposal pit, and (C) thermal and hydraulic boundary conditions in compacted barrier. 1. Host rock; 2. Compacted blocks; 3. Technical gap between blocks; 4. Gap between compacted blocks and host rock; 5. Waste canister. H, hydration from host rock; T, applied temperature.



mechanical response (axial and radial stresses) of the materials are monitored with an elapsed time. The development of stresses due to thermal and thermohydraulic loading are usually measured at the low-temperature end (fig. 1C), whereas the water content, volumetric, and chemical properties of the tested materials are determined after termination of the tests (Villar et al. 2005; Tripathy, Thomas, and Bag 2015).

During the early phase of the repository lifetime, the impact of thermal loading on the hydromechanical behavior of the materials is of significant interest (Sellin and Leupin 2013; Tripathy, Thomas, and Stratos 2017). A difference in the temperature between the high-level waste canisters and the surrounding barrier materials tends to cause redistribution of the water content leading to volumetric contraction and expansion of the materials. Under the confined condition, development of swelling pressure occurs, which, in turn, provides the desired structural stability to the repositories (Pusch and Yong 2006). The magnitude of swelling pressure that gets developed during the thermal loading phase depends upon the vapor-phase continuity in the system and the stiffness of the boundary (restraint), which may differ in both axial and lateral directions (fig. 1C). Therefore, an understanding of the coupled processes in the repositories on account of thermal loading demands measurements of the axial total stresses at both warmer and cooler regions, the lateral stress, and simultaneous measurements of the water content. These aspects have not been explored in detail in the past.

An innovative column-type experimental test setup was designed and fabricated at Ruhr-Universität Bochum, Germany, for investigating the coupled THM behavior of expansive soils. The paper presents the technical details of the functional components, monitoring sensors, and instrumentation for transient measurements of various key parameters. System implementation and validation tests were performed under an applied temperature gradient. A test was performed on a sample of compacted Calcigel bentonite-sand mixture (50:50) to investigate the response of the material under an applied temperature gradient.

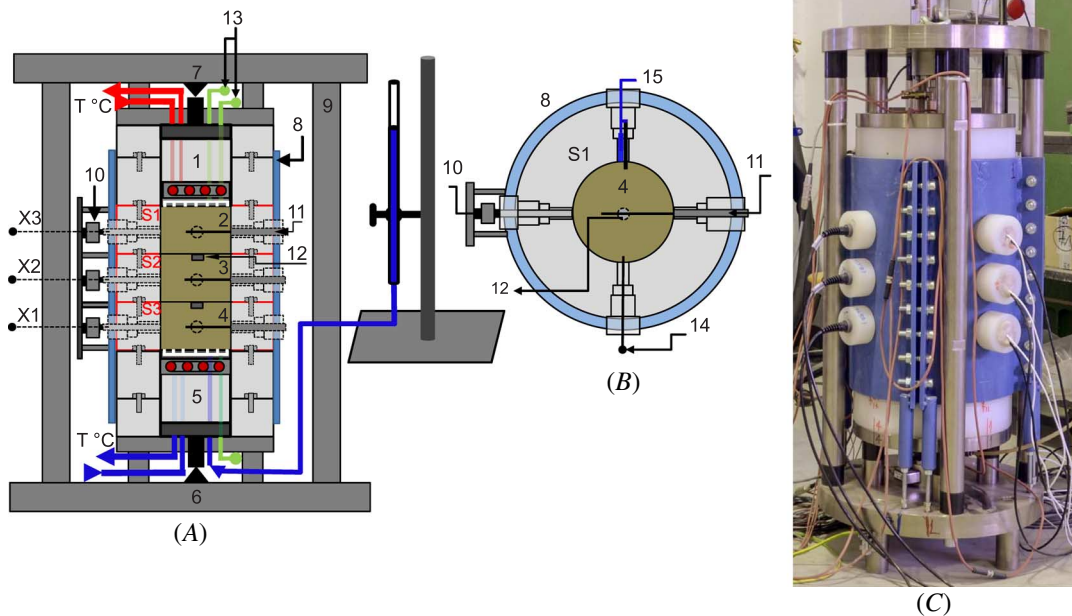
New Column-Type Device

Figure 2 shows the constructional details of the newly designed column-type test device. The device is composed of top and bottom plugs (items 1 and 5 in fig. 2A), sample rings (items S1, S2, and S3 in fig. 2A), and a confining cell (item 8). A rigid frame (item 9) provides the restraint along the axial direction. The stresses in the axial direction are measured using the load cells (items 6 and 7). The test setup allows testing cylindrical soil samples (diameter [dia.] = 150 mm and height = 300 mm) and provides 3 measurement sections located at various heights from the bottom of the sample, such as X1 (50 mm), X2 (150 mm), and X3 (250 mm) (fig. 2A).

The top and bottom plugs have the same constructional features for applying the thermal gradients along the height of soil sample (Rawat 2019). The plugs were made of a polyvinylidene fluoride (PVDF) cylinder (dia. = 148 mm and height = 100 mm) with a stainless steel chamber (dia. = 150 mm and thickness = 20 mm) attached to one face. The chamber accommodated a heating/cooling coil, which, in turn, was connected to an external thermostat (not shown in fig. 2) and a sintered porous stainless steel disk (dia. = 150 mm and thickness = 10 mm). The opposite face of the PVDF cylinder contained a cylindrical stainless steel plate (dia. = 148 mm and height = 25 mm) with a central loading plunger (dia. = 60 mm and height = 80 mm) and facilitated connections for a water inlet and an air outlet that can be used in case of thermo-hydraulic tests. The temperature at either end is controlled by circulating silicon oil in the coil with the precision of 0.1°C. The integrated design of the stainless steel chamber with the porous disk provided an adequate thermal equilibrium between the heating and hydration systems. The plugs acted as pistons to transfer load to the load cells located at both ends of the device. The PVDF piston assemblies provided the required thermal insulation for the heating unit located within the plugs.

To accommodate the soil sample, 3 PVDF encapsulation rings/sample rings (outer dia. = 350 mm, inner dia. = 150 mm, and height = 100 mm) were used (i.e., S1, S2, and S3) (fig. 2). The PVDF sample rings assembly provided the mechanical stability, an adequate thermal insulation in the lateral direction, and accommodated the ports for the components of the monitoring sensors. Compacted samples (items 2, 3, 4) can be prepared by compacting soil-water mixtures in a separate compaction mold and further transferred to the sample rings. Each sample ring had four holes at the mid height, but radially positioned at an angle of 90° for installing

FIG. 2 Constructional details of the newly designed column-type experimental setup, vertical (A) and horizontal (B) sectional views, and (C) a photograph of the device. 1. Top plug; 2-4. Compacted blocks; 5. Bottom plug; 6. Bottom load cell; 7. Top load cell; 8. Confining cell; 9. Rigid frame; 10. Radial load cells; 11. TDRs; 12. Pressure transducer; 13. Top air vent; 14. Pt100 sensor; 15. RH sensor with additional Pt100 probe. S1, S2, and S3, sample rings.



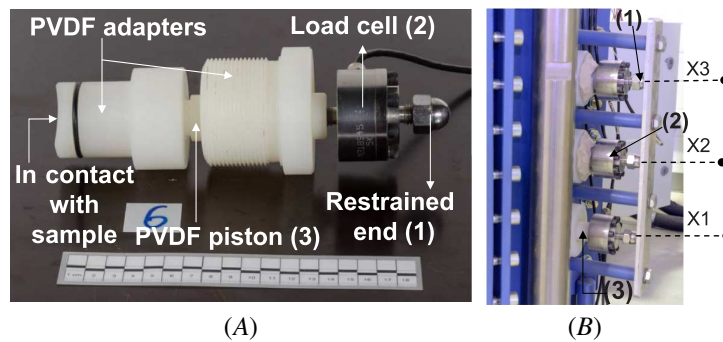
the sensors, that facilitated measuring temperature, relative humidity (RH), water content, and lateral total stress (fig. 2B). The sensors were installed with their respective PVDF adaptors (fig. 2C) for minimizing the heat loss and any possible disturbances to the electronics of the sensors. The provision of O-ring connections along with tightening screws that were made of PVDF provided the air/watertight joints between two consecutive sample rings (fig. 2A). A stainless steel confining cell (item 8, fig. 2A) was used to provide additional resistance against the outward lateral deformation of the sample rings during a test. Additionally, the confining cell facilitated the installation of the lateral load cells (fig. 3). A vertical stainless steel plate was used to provide the restraint for the lateral load cells (fig. 3B). Because of the presence of technical voids (i.e., the spaces created between compacted soil samples and the embedded sensors), the stiffness of the measuring system can be expected to be less in the axial direction than in the lateral direction. This may, in turn, influence the development of the total stress during a test.

SENSORS AND INSTRUMENTS USED

Table 1 shows the type of sensors and the instruments used in this study. For each case, the measurement range and accuracy are shown. The accuracies of the relative humidity and water content sensors are expected to affect the interpretation of test results, particularly so when the variations of these parameters are close to the accuracy limits of the sensors. The load cells used for measuring the total stresses at top and bottom of the sample and the lateral load cells for measuring the lateral stresses were installed outside the cell for minimizing the impact of temperature on the measurements (figs. 2 and 3). The load cell measurements (kN) were converted to the stress unit (MPa) for the sake of presentation. The Pt100 sensors, relative humidity sensors, top and bottom load cells, and the lateral load cells were received with the factory calibration certificates. Additional tests were carried out to verify the accuracy of the relative humidity sensors using saturated salt solutions of lithium chloride, sodium chloride, and potassium sulfate. The measured relative humidity values agreed very well with the specified values (ASTM E104-20a, *Standard Practice for Maintaining Constant Relative Humidity by Means of Aqueous Solutions*).

FIG. 3

Lateral load cell installation details. (A) Load cell along with accessories and (B) installation at measurement sections X1, X2, and X3 along the height of sample.


TABLE 1

Details of the monitoring sensors and instruments used with the device

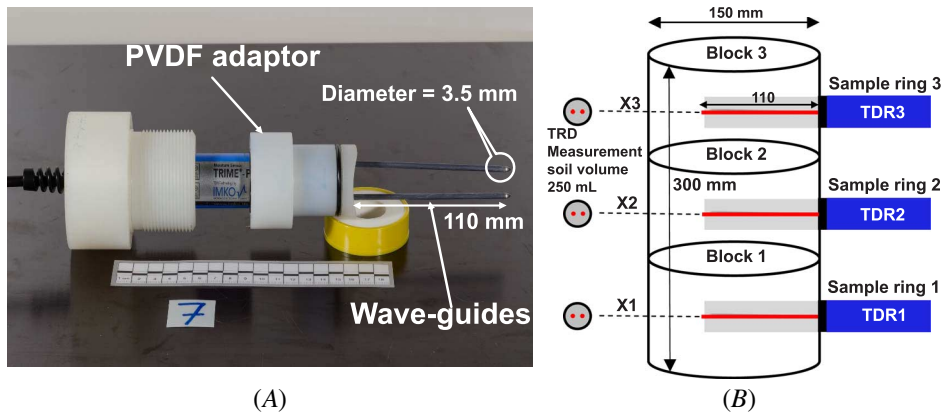
Measuring Parameter and Sensor Type (1)	Number of Units (2)	Installation Remark (3)	Measurement Specifications (3)	Accuracy (4)
Temperature (Pt100)	5	At sections X1, X2, and X3 (3 nos.), at top and bottom plugs (2 nos.); sensor dia. = 3 mm, embedment length = 10 mm.	-40°C to 200°C	$(0.1 + 0.0017 \times t)$ °C
Relative humidity (VAISALA HMT337 with heating option)	3	In closed vapor chambers at sections X1, X2, and X3. Additional Pt100 probe embedded in the sample up to 10 mm.	0 to 100 % RH	$\pm(1.5 + 0.015 \times \text{reading})$ % RH
Water content (IMKO PICO-32)	3	At sections X1, X2, and X3.	0 to 70 %	± 2 % for 0–40 % ± 3 % for 40–70 %
Lateral stress (OMEGA Eng.: LCM-203)	3	At sections X1, X2, and X3.	5 kN	± 0.3 % including nonlinearity, hysteresis, and repeatability.
Axial stress (OMEGA Eng.: LCM-402)	2	At top and bottom ends	100 kN	Same as above in lateral stress.
Axial pressure (KYOWA-BEC pressure transducer)	2	At the interfaces between the compacted soil blocks 2-3, and 3-4.	1 MPa	± 0.03 MPa (incl. nonlinearity and hysteresis with additional ± 0.4 %/°C due to T-effect
Thermostats (Huber Ministat 230 and CC-202)	2	External unit	20°C to 95°C	Temperature stability = ± 0.02 °C
Data logger (Graphtech-820)	1	External unit	20 channels	...

Two pressure transducers (item no. 12 in [fig. 2](#)) were embedded in the sample to measure the axial stresses at heights of 100 mm (B1) and 200 mm (B2) from the base of the sample. These pressure transducers were anticipated to operate at elevated temperatures. For these pressure transducers, as suggested by the supplier, a thermal drift of ± 0.4 %/°C in terms of the measured voltage for a temperature range of 24°C to 60°C was considered for obtaining the actual pressures.

TIME DOMAIN REFLECTOMETRY SENSOR CALIBRATION

The time domain reflectometry (TDR)-based sensors ([fig. 4](#)) were used for measuring the water content of soil sample during a test. The sensor constitutes of two parallel wave guides or probes (dia. = 3.5 mm and length = 110 mm) made of stainless steel and are coated with polyvinyl chloride for waterproofing. For correct measurements of the water content, the entire length of the probes must be embedded in the soil sample. The wave guides

FIG. 4 TDR sensor installation details. (A) TDR along with accessories and (B) a schematic showing positions of the sensors along the height of sample.



are sensitive to deformation. In the device, the TDR sensors were installed with their respective PVDF adaptors (fig. 4A). Figure 4B presents a schematic of a sample along with the positions of the TDR sensors.

The TDR probes generate a high-frequency pulse (up to 1 GHz) that propagates along the wave guides, thereby generating an electromagnetic field. At the end of the waveguides, the pulse is reflected to the source. The transit time (t_p) depends upon the dielectric properties of the medium in which the measurement is carried out. It is usual practice to establish the calibration curve (i.e., t_p versus water content) for the material under consideration at various temperatures of interest (Topp, Davis, and Annan 1980; Schanz, Baille, and Nguyen-Tuan 2011). The minimum sample volume for water content measurement is usually 250 cm³.

For establishing the TDR calibration curve in this study, laboratory tests were carried out on compacted bentonite–sand mixture (50:50) at 3 different initial water contents (5, 10, and 15%). Samples (dia. = 150 mm and height = 100 mm) were prepared by statically compacting the mixtures to attain an average dry density of 1.92 Mg/m³. After the extrusion of the compacted samples from the compaction mold, the samples were covered with layers of plastic film, aluminum foil, and plastic adhesive tape to prevent the moisture loss during the calibration tests. The calibration tests were performed at room temperature and at several elevated temperature levels between 25°C and 60°C in a temperature-controlled drying oven. The maximum temperature (i.e., 60°C) corresponds to the limit of measurement of the TDR probe. The waveguides of the sensors were inserted in the predrilled holes in the compacted samples. A Pt100 sensor was used to measure temperature during the tests. All measurements were performed after the samples attained the desired temperatures. Based on the test results and using an interpolation technique, the calibration test data were plotted as a 3-D surface (fig. 5) with three variables, such as water content, temperature, and transit time (t_p). A MATLAB program was developed to extract the actual water content from the measured value of t_p corresponding to any given temperature.

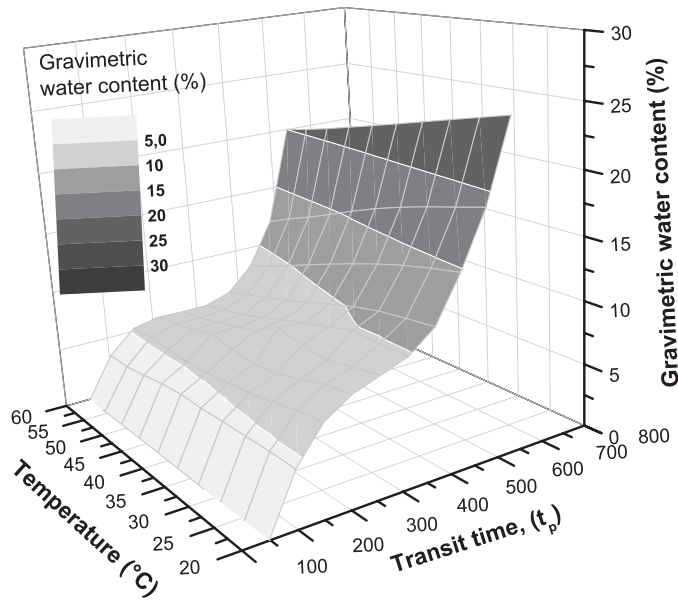
Preliminary Tests

RESPONSE OF LOAD CELLS UNDER PRESSURE AND THERMAL LOADING CONDITIONS

Prior to the main test with a sample of compacted bentonite–sand mixture, a series of tests was performed using the device to examine the air and water tightness of the constructional joints, to study the response of the load cells, and further for quantifying the temperature-induced volumetric deformation of the test setup at an elevated temperature. For the first two aspects, a test was carried out by using an oak wood dummy sample (dia. = 100 mm and length = 300 mm). A schematic of the test setup is shown in figure 6. The applied temperatures at the opposite ends of the wooden sample were 80°C at the top and 20°C at the bottom. The applied temperature

FIG. 5

Calibration curve of the TDR sensors as applicable to the compacted sand-bentonite mixture (50:50) used in this study.

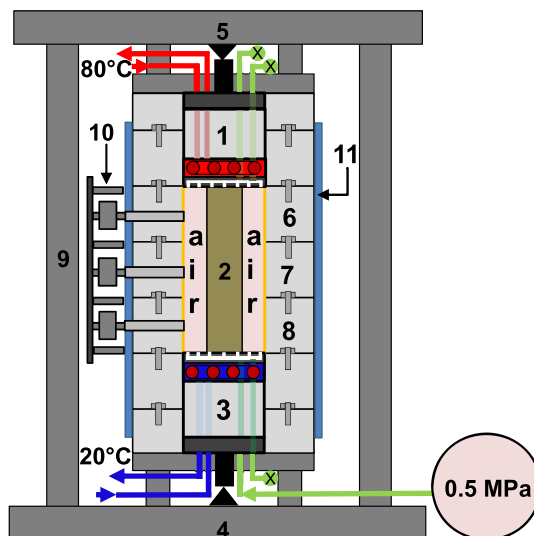


gradient was 0.2°C/mm. A choice of the elevated temperature of 80°C ties up with the temperature adopted in case of testing the compacted bentonite–sand mixture sample. The wooden dummy sample was placed between the top and bottom plugs that prevented the top plug to retreat into the cell cavity. The dummy also served as an insulator between the top and bottom ends. The difference in the diameters of the PVDF sample rings and the wooden dummy created an annular space surrounding the dummy (fig. 6).

Considering the thermal properties of oak wood (thermal conductivity = 0.14 W/mK, coefficient of linear thermal expansion = 4.86×10^{-6} m/mK parallel to grain) (Avalone and Baumeister 2017), it was expected that the dummy would expand under thermal loading and thus, would exhibit an axial stress under restrained

FIG. 6

A schematic view of the test setup for verifying response of load cells under pressure and thermal loading conditions. 1. Top plug; 2. Wooden dummy; 3. Bottom plug; 4. Load cell (bottom); 5. Load cell (top); 6–8. PVDF sample rings; 9. Rigid frame; 10. Radial load cells; 11. Confining cell; X = Air/ water inlet closed.



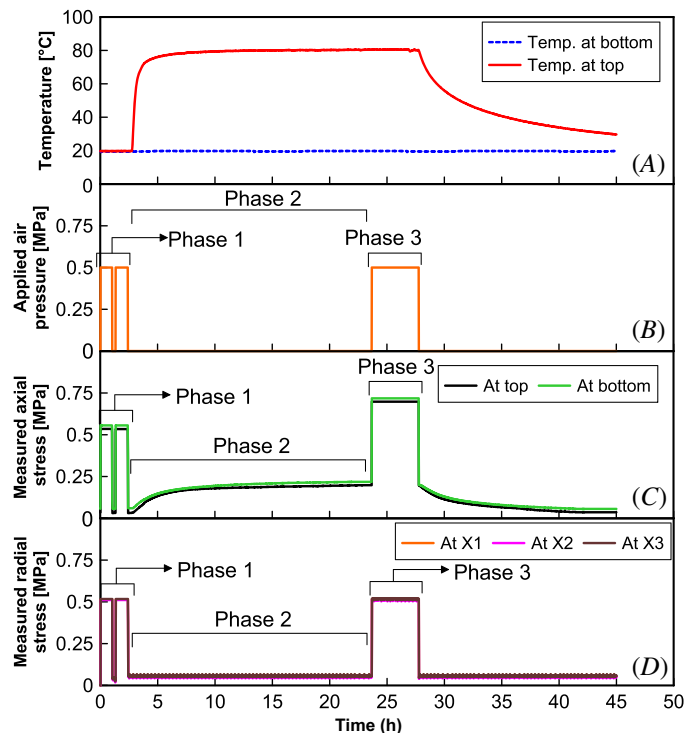
condition. The axial load cells measured the stresses at the top and bottom of the wooden dummy sample. Pressurized air was supplied from an external air compressor to the annular space between the sample and the inner surface of the sample rings for verifying the response of the load cells. The lateral load cells measured the applied air pressure at sections X1, X2, and X3 (fig. 2).

The test with the wooden dummy was conducted in three phases as depicted in figure 7. Prior to the commencement of the test, the seating pressures for the axial and lateral load cells were 0.06 and 0.04 MPa, respectively. The applied seating pressure in the axial direction ensured proper contact between the axial load cells and the wooden dummy. The seating pressure in the lateral direction was developed during the installation of the lateral load cells. In phase 1, the annular space between the PVDF sample rings and wooden dummy was subjected to two successive cycles of compression–decompression using an air pressure of 0.5 MPa at room temperature. The applied air pressure at the end of phase 1 was zero. In phase 2, the temperature at the top was raised to 80°C, whereas it was kept constant at 20°C at the opposite end of the sample. No air pressure was applied during this phase. In phase 3, the temperature at top and bottom remained at 80°C and 20°C, respectively, whereas the air pressure was raised to 0.5 MPa and kept constant for a period of 5 h. At the end of phase 3, the heating process was terminated, and the air pressure was reduced to zero.

The applied temperatures at both ends of the wooden dummy and the air pressure are shown in figure 7A and 7B, respectively. Figure 7C and 7D shows the measured axial stresses at both ends of the sample and the radial stresses at the three predetermined levels on the circumference of the cell, respectively. As can be seen in figure 7, the measured axial and radial stress values are similar and agree well with the applied air pressure of 0.5 MPa during phase 1. The load cells responded well when the air pressure was reduced to zero. In phase 2, the measured stresses by the top and bottom load cells were on account of the temperature-induced stresses due to the thermal expansion of the wooden dummy because the applied air pressure was zero. The measured axial stresses at the top and bottom ends were about 0.22 MPa (fig. 7C). As expected, the stresses measured by the lateral load cells were at seating pressure of 0.04 MPa (fig. 7D) during phase 2. In phase 3, the air pressure

FIG. 7

Response of load cells to pressure and thermal loadings in the presence of a dummy wood sample. (A) Applied temperature at opposite ends of the dummy, (B) applied air pressure, (C) measured axial total stress, and (D) measured lateral total stress.



in the annular space was increased to 0.5 MPa and further decreased. This occurred when the elevated temperature was applied at the top end. The top and bottom load cells responded well to the elevated air pressure (fig. 7C). The measured axial stress value at both ends of the sample was about 0.72 MPa, whereas a net increase in the pressure of 0.5 MPa was noted for the lateral load cells. The test results clearly showed that the device functioned well with no leakage significant enough to override the applied air pressure and further, the load cells responded well to the elevated temperature and pressure conditions.

VOLUMETRIC THERMAL EXPANSION AT ELEVATED TEMPERATURE

One of the major issues in the soil testing at elevated temperature and under the K_0 condition is the volumetric thermal expansion of test setup that may contribute to the changes in the stress state of the tested soil sample. Tests were conducted in the device to quantify the volumetric thermal expansion of the test setup at a temperature of 80°C. To investigate the effect of elevated temperature on thermal expansion of PVDF sample rings, two tests were performed, such as with and without the confining cell.

Figure 8 shows a schematic of the test setup. A cylindrical stainless steel dummy (dia. = 100 mm and height = 300 mm) was placed between the top and bottom plugs. The steel dummy provided the mechanical support to the top plug. The annular space between the PVDF sample rings assembly and the steel dummy was filled with water using the bottom inlet port, whereas all other air/water inlets were kept closed. Sufficient care was exercised to remove the trapped air bubbles by allowing water to flow from bottom to top. Two water-filled burettes were connected to the water inlet port (fig. 8), and the water level in the burettes was kept at the level of water inside the cell. A fluctuation of temperature in the laboratory may cause evaporation of water, which, in turn, can significantly affect the volume measurements using the burettes. To minimize the evaporation of water in the burettes, the exposed water surfaces in the burettes were covered with a lubricant oil. The temperature at both the ends of the steel dummy was raised to 80°C using a separate external heating unit. The water level in the parallel-burette system was monitored continuously for a period of more than 96 h. In both tests (i.e., with and without the confining cell), the water levels in the burettes were found to be higher than the initial levels, indicating that water flow occurred from the cell to the burettes.

Because of a rise in the temperature to 80°C, an expansion of the stainless steel dummy and the PVDF sample rings assembly, and an increase in the water volume in the annular space are expected. Note that the PVDF sample ring assembly was subjected to a temperature gradient along the wall thickness (i.e., 80°C on the inner

FIG. 8

A schematic view of the test setup for quantifying the volumetric thermal expansion of the device in the presence of a stainless steel dummy. 1. Load cell (top); 2. Top plug; 3. Steel dummy; 4. Water; 5. Bottom plug; 6. Load cell (bottom); 7–9. PVDF sample rings; 10. Confining cell; 11. Rigid frame. X, air/water inlet closed.

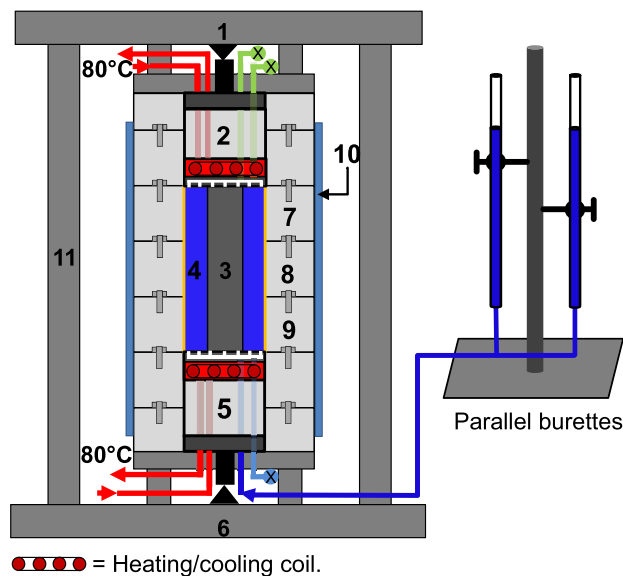


TABLE 2

Volumetric expansion of PVDF samples ring assembly

Description (1)	Values (2)
Initial volume of steel dummy ($\times 10^3 \text{ mm}^3$)	2,356.19
Volumetric expansion of steel dummy at 80°C ($\times 10^3 \text{ mm}^3$)	6.78
Initial volume of water ($\times 10^3 \text{ mm}^3$)	2,945.21
Volumetric expansion of water at 80°C ($\times 10^3 \text{ mm}^3$)	37.81
Cumulative volumetric expansion ($\times 10^3 \text{ mm}^3$)	44.59
Measured volume change ($\times 10^3 \text{ mm}^3$)	42.20 (42.60) ^a
Calculated volumetric expansion of sample rings assembly ($\times 10^3 \text{ mm}^3$)	2.39 (1.99) ^a

Note: ^a Value within brackets is for the case without the confining cell.

surface and the ambient laboratory temperature of 22°C on the outer surface). The combined effect of an expansion of various components is expected to affect the water levels in the burettes. For example, an increase in the volume of the stainless steel dummy and the water in the annular space would cause an increase in the water levels in the outside burettes. An expansion of the PVDF sample rings assembly would cause an increase in the internal diameter leading to a drop in the water level in the burettes.

In order to quantify the thermal expansion of the PVDF rings assembly, calculations were made in which the volumetric thermal expansion of the stainless steel dummy and water was calculated at the applied temperature of 80°C by considering the appropriate values of coefficient of volumetric thermal expansion of steel ($\alpha_{\text{steel}} = 4.80 \times 10^{-5} \text{ 1/}^\circ\text{C}$) and water ($\alpha_{\text{water}} = 2.14 \times 10^{-4} \text{ 1/}^\circ\text{C}$). **Table 2** shows the initial volume and the volume increase due to the thermal expansion of the stainless steel dummy and water and the measured volume change based on the burette readings. It can be seen in **Table 2** that the measured water volume was slightly less than the calculated values in both tests. This clearly suggests that an expansion of the PVDF sample rings assembly occurred (about $2.39 \times 10^3 \text{ mm}^3$ and $1.99 \times 10^3 \text{ mm}^3$), which is about 0.04 % of the initial internal volume (dia. = 150 mm and height = 300 mm). The volume of water in the cell during the test was 55.5 % of the total volume. The actual testing involves a soil sample filling the PVDF sample ring. Considering that the coefficient of thermal expansion of compacted bentonite is about $2 \times 10^{-4} \text{ 1/}^\circ\text{C}$, the error due to the thermal expansion during tests on bentonite at 80°C would increase to 0.07 %, which may be considered insignificant in terms of its contribution to the interpretation of the test results.

TEST WITH COMPACTED BENTONITE-SAND MIXTURE

A test was performed with compacted Calcigel bentonite-sand mixture (50:50) under an applied temperature gradient. The testing conditions mimic the early phase lifetime of underground repositories during which the thermal loading is considered significant.

Calcigel bentonite contains 60–70 % montmorillonite with calcium and magnesium as major exchangeable cations. The specific gravity, liquid limit, and plastic limit of the bentonite are 2.80, 180, and 45 %, respectively. Calcigel bentonite powder and oven-dried fine sand were weighed separately with an equal dry mass at room temperature. The initial water content of Calcigel bentonite was 6 %. The initial water content of the mixture was raised to 9 % by adding the required amount of water. The bentonite-sand-water mixture was placed in a sealed plastic bag and stored in an airtight container for 28 days for homogeneous distribution of moisture. The initial total suction of the mixture was measured by using a chilled-mirror dew-point potentiometer and was found to be 26.9 MPa.

Three compacted samples to be accommodated in sample rings S1, S2, and S3 were prepared. The diameter and height of each samples were 150 and 100 mm, respectively. Each sample was prepared by statically compacting the bentonite-sand-water mixture in a sample mold in three layers by applying a static compaction pressure of 30 MPa using a uniaxial static compaction machine to achieve a dry density of 1.93 Mg/m^3 . Prior to

compacting the first layer in case of samples for rings S2 and S3, a steel dummy having similar dimensions to the pressure transducer was placed at the center of the base plate for creating the desired space for the embedded load cells (KYOWA-BEC in Table 1) (fig. 9). The surface of the compacted layer was scarified prior to placing the next layer to ensure homogeneity between the layers. After completion of the compaction process, the samples were extruded from the compaction mold. The dummy was removed in case of samples for rings S2 and S3 for the installation of the pressure transducers (fig. 9). The pressure transducers were located at height of 100 and 200 mm from the base of the sample. The compacted samples were then prepared for installing the monitoring sensors. For installing the TDR waveguides, two holes (dia. = 3.2 mm and length = 110 mm) at predetermined positions were drilled (figs. 2 and 4). Similarly, two holes, each with 10-mm length, were also drilled for installing the Pt100 sensors.

The sample rings with compacted samples and the monitoring sensors in appropriate positions were then assembled and positioned in the load frame. The confining cell was mounted, and the lateral load cells and the lateral restraint were installed. The air and water vents located at top and bottom of the cell were kept closed (fig. 2C). To achieve good contact between the top and bottom load cells and the sample, the stiffness of the horizontal bar of the load frame was adjusted to apply a seating stress (fig. 2). Similarly, good contact between the sample and the lateral load cells was achieved by tightening the bolts on the vertical stainless steel plate and screwing the PVDF adapters to the PVDF sample rings (figs. 3 and 9). Table 3 (column 2) shows the seating stresses measured by the load cells and the embedded pressure transducers. The installation stresses (i.e., the seating stresses) measured by the top and bottom load cells were the same (0.34 MPa). The lateral stresses were different at all levels with a mean stress and standard deviation of 1.3 and 0.07 MPa, respectively. The response of the two embedded transducers was dissimilar with 0.03 MPa at a height of 100 mm and 0.20 MPa at a height of

FIG. 9 (A) A photograph of compacted bentonite–sand mixture sample (1. Side view of sample for ring S1 or S2 or S3; 2. Top view of sample for ring S2 or S3 with the seating space for a miniature pressure transducer), and (B) a photograph of PVDF ring S2 or S3 with sample showing pressure transducer installation.

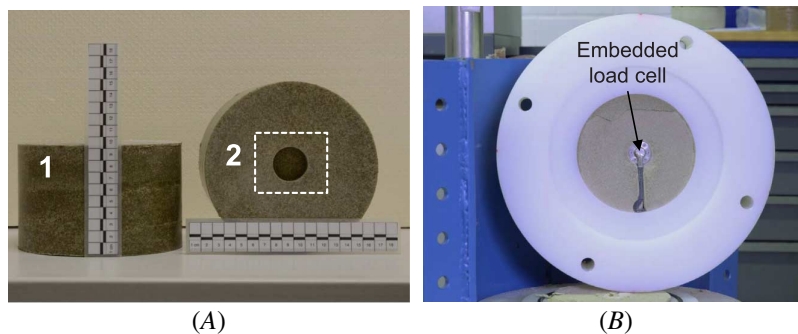


TABLE 3

Measured axial and radial stresses during equilibration period and thermal loading

Location of Load Cell/ Pressure Transducer (1)	Seating Stress, MPa (2)	At the end of Equilibration Period, MPa (3)	One Day after Thermal Loading, MPa (4)	At Termination of the Test, MPa (5)
Bottom	0.33	0.34	0.70	0.47
Embedded at height 100 mm	0.03	0.02	0.10	0
Embedded at height 200 mm	0.20	0.16	0.38	0.35
Top	0.34	0.42	0.84	0.76
Section X1 (lateral)	1.28	1.24	1.88	0.59
Section X2 (lateral)	1.24	1.30	1.24	1.63
Section X3 (lateral)	1.40	0.96	0.68	2.51

200 mm. The applied seating stresses were kept at positive values, because a reduction of dimensions of the sample due to thermal loading would get reflected on a reduction in the stress values.

The sample was tested by applying a temperature of 80°C at the bottom end and 20°C at the top end. The test was conducted for a period of 92 days (35 days of equilibration period, the last 8 days of which are presented in the respective diagrams of temperature, relative humidity, water content and stress versus time, and 57 days of thermal loading period). The equilibration period was considered to allow redistribution of water content and relative humidity (suction) within the sample. Studies in the past have shown that compacted expansive soils exhibit stresses due to the relaxation of the static compaction stress and particle rearrangement (Subba Rao and Tripathy 2003; Tripathy, Bag, and Thomas 2014). Therefore, changes in the stress were monitored during the equilibration period. Although the data acquisition was made during the entire equilibration period, only the data corresponding to the last 8 days of equilibration period are presented, during which some changes in the stresses were observed. Prior to applying the thermal loading, the air vent located at the top end of the device was opened. This allowed a release of the water vapor from the sample during the test. Therefore, a constant moisture condition within the sample did not exist.

Test Results and Discussion

TEMPERATURE

Figure 10 shows the elapsed time versus temperature plot. The measured temperatures during the last 8 days from the 35-day equilibration period are presented. The commencement of the thermal loading is indicated in **figure 10**. A temperature gradient between top and bottom of the sample of 0.2°C/mm was applied at the end of the equilibration period. A temperature equilibrium was attained at all the salient levels within a day after the commencement of thermal loading.

The temperature profiles and the calculated temperature gradients along the height of the sample at different times after the commencement of thermal loading (0, 1, and 57 days) are shown in **figure 11**. The temperature gradient was calculated based on the difference in the temperature at the heat source and at any measurement section and the distance of that section from the heat source. The temperature gradient was found to be about 0.40°C/mm at section X1 (50 mm from the heat source), which decreased to about 0.22°C/mm nearer to the top end (i.e., at section X3, 250 mm from the heat source). Tripathy, Thomas, and Stratos (2017) have reported similar trends for the temperature gradient for tests at 85°C and 150°C. The test results by the researchers have brought out the influence of thermal insulation on the lateral heat loss and its effect on the distribution of temperature along the height of compacted bentonite samples. It is evident from the test results in this study that the lateral

FIG. 10

Elapsed time versus temperature plot for the test with the compacted sand-bentonite mixture.

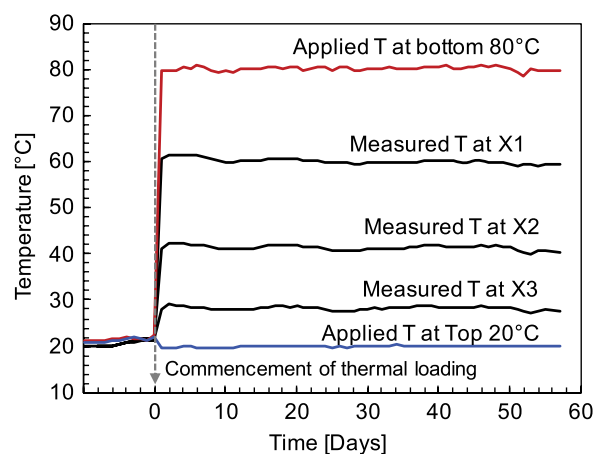
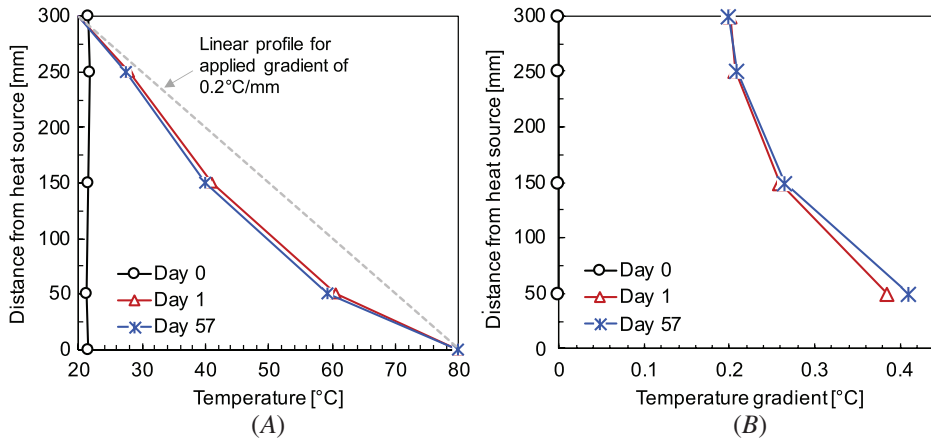


FIG. 11 (A) Temperature profile and (B) temperature gradient at 0, 1, and 57 days.



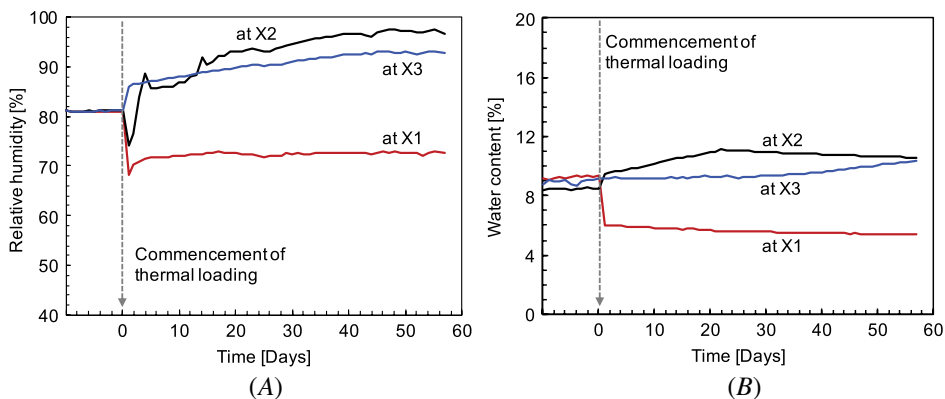
heat loss along with the changes in the soil thermal conductivity on account of the changes in the water content (as shown in the following sections) affected the temperature distribution in the compacted sample.

RELATIVE HUMIDITY AND WATER CONTENT

Figure 12A and 12B shows the measured relative humidity and water content in the sample with elapsed time at sections X1, X2, and X3. Figure 13A and 13B shows the profiles of relative humidity and water content, respectively. The test results presented in figure 13 are corresponding to the elapsed times of 0, 1, and 57 days after the commencement of thermal loading. At the end of equilibration period of 35 days (shown as day 0 in fig. 12A), the measured relative humidity at all sections was found to be similar (about 81 %). Similarly, at the end of equilibration period, the difference between the water contents at any two sections remained within ± 0.5 % (compaction water content = 9 %) (fig. 12B).

Within a day from the commencement of thermal loading, a decrease in the relative humidity occurred at sections X1 and X2 (i.e., from 81 % to 68 % at X1 and from 81 % to 74 % at X2), whereas the relative humidity increased to 86 % at section X3 (fig. 12A). During this period, the water content at section X1 decreased from 9.1 % to about 6 %, whereas it increased from 8.5 % to 9.2 % at section X2 and remained nearly unchanged (9.1 %) at section X3 (fig. 12B).

FIG. 12 (A) Elapsed time versus relative humidity and (B) elapsed time versus water content plots.



The short-term effect of thermal loading may be considered to initiate several phenomena within unsaturated porous media. At a constant amount of water vapor in the air space, an increase in the temperature causes a decrease in the relative humidity. Additionally, an increase in the temperature causes thermal dilation of the medium, generation of gas pressure, and flow of water vapor from the warmer to the cooler regions. A decrease in both the relative humidity and water content at section X1 suggests that the part of the sample closer to the heat source underwent drying process accompanied by a thermal dilation as will be shown in the next section both axial and lateral stresses increased during this period. An increase in the water content and a decrease in the relative humidity at section X2 within 1 day from the commencement of thermal loading can be attributed to the combined effect of two phenomena, such as (1) moisture flow from the regions closer to the heat source toward section X2 that caused an increase in the water content and (2) an increase in the temperature at section X2 caused thermal dilation that reduced the relative humidity (Fredlund, Rahardjo, and Fredlund 2012). The test results showed that the thermal dilation effect was dominant at section X2 immediately after the commencement of thermal loading. At section X3, although the amount of water vapor increased, as shown by an increase in the relative humidity; however, an increase in the temperature at X3 to about 30°C and a release of the water vapor via the vent located at the top of the cell did not permit the condensation of water molecules to occur, which would cause a change in the water content.

Beyond 1 day of the commencement of thermal loading, the relative humidity at section X1 increased from 68 % to 72 % and further remained constant, whereas the water content decreased gradually from 6.0 % to about 5.5 % until termination of the test. The relative humidity at sections X2 and X3 increased and attained 97 % and 93 %, respectively. The water content at section X2 linearly increased from 9.2 % until a maximum value of 11.2 % at day 22 and subsequently decreased to 10.6 %. The water content at section X3 remained nearly constant at about 9.2 % until day 32, followed by an increase to the final value of 10.3 %. The increase in the water content at section X3 occurred at a much slower rate as compared with that at section X2.

The long-term effect of thermal loading tends to provide a dynamic equilibrium condition in the unsaturated porous media. The water vapor flow from hotter to cooler regions due to a thermal gradient and the liquid water flow in opposite direction (usually downward) due to a suction gradient cause redistribution of suction and water content. An increase in the relative humidity at section X1 beyond 1 day after the thermal loading may be attributed to the redistribution of vapor pressure toward attaining the dynamic equilibrium condition. An increase in the water content at section X3 at slower rate as compared with that occurred at section X2 can be attributed to the release of water vapor at the top end. In a closed system (i.e., without any provision to vent water vapor at the opposite end of heat source), the water content generally increases linearly with an increasing distance from the heat source (Tripathy, Thomas, and Stratos 2017).

The profiles of the temperature (fig. 11A), relative humidity (fig. 13A), and water content (fig. 13B) clearly indicate that a steady state temperature profile was established at a shorter time than the relative humidity and water content profiles. Similar results from tests on compacted bentonites have been reported in the past (Tripathy, Thomas, and Bag 2015; Tripathy, Thomas, and Stratos 2017).

AXIAL AND LATERAL STRESSES

Figure 14A and 14B shows the axial and lateral stresses at various salient levels of the sample both during the equilibration period (only the last 8 days of data from the 35-day equilibration period are shown) and further, the changes in these stresses that occurred due to the application of the thermal loading. Table 3 (columns 3 to 5) shows the stresses measured by the load cells and the embedded transducers at the end of equilibration period, 1 day from the commencement of thermal loading and at the time of termination of the test. The changes in the axial and lateral stresses at various levels due to thermal loading for the durations of 1 and 57 days are shown in figure 15.

During the equilibration period, the axial stress increased by 0.01 MPa at the bottom and 0.08 MPa at the top, whereas the stresses at heights 100 mm and 200 mm decreased by 0.01 and 0.04 MPa, respectively (Table 3). Similarly, the lateral stress decreased at sections X1 and X3 by 0.04 and 0.44 MPa, respectively, whereas it increased at section X2 by 0.06 MPa (Table 3). The results suggest that a release of post-compaction residual stress

FIG. 13 Profiles of (A) relative humidity and (B) water content.

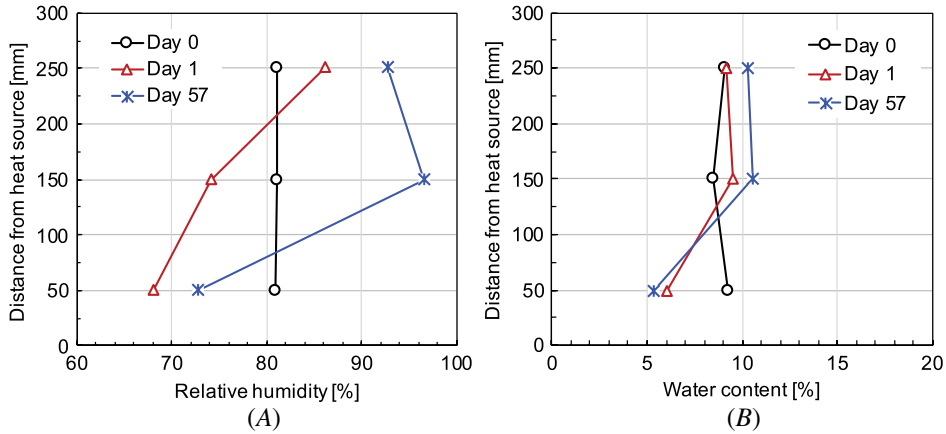


FIG. 14 Development of (A) axial stress and (B) lateral stress at various salient levels of the sample.

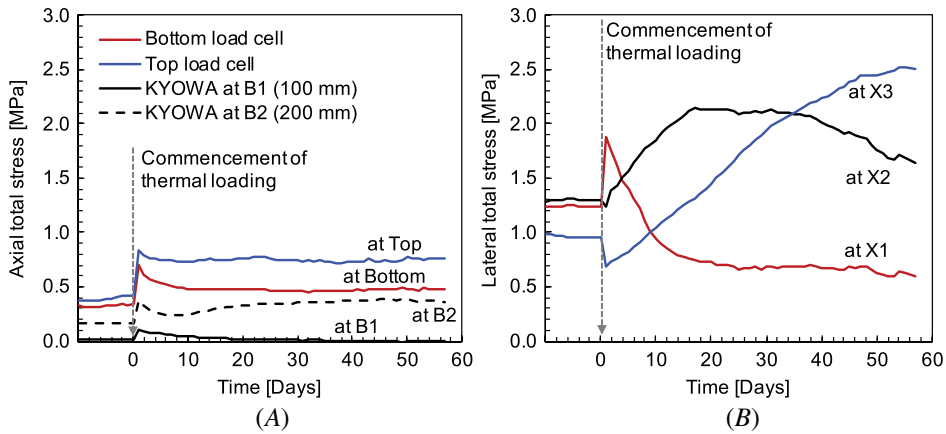
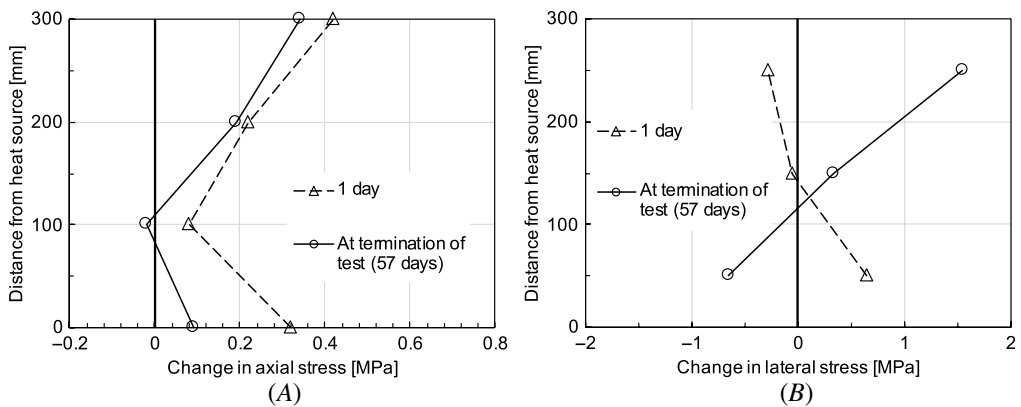


FIG. 15 Changes in the (A) axial stress and (B) lateral stress at various levels due to thermal loading.



(Tripathy, Bag, and Thomas 2014) occurred with time at a constant water content, leading to an increase in the axial stress in the direction opposite to that of the compaction stress which, in turn, caused a reduction in the lateral stress. The other factors that may contribute to the changes in axial and radial stresses are the particle rearrangement with time at a constant water content (Subba Rao and Tripathy 2003), redistribution of water content following the compaction process, and redistribution of stress due to the presence of voids at the interfaces between the compacted samples and between the sample, the sensors, and the pressure transducers.

Within a day from the commencement of thermal loading, the measured axial stresses at top, bottom, and within the sample were found to increase (fig. 14A). The increase in the axial stress at the bottom, at a height of 100 mm, at a height of 200 mm, and at the top were 0.36, 0.08, 0.22, and 0.42 MPa, respectively (columns 3 and 4 in Table 3 and fig. 15A). The lateral stress at section X1 increased by 0.64 MPa, whereas at sections X2 and X3, it decreased by 0.06 and 0.28 MPa, respectively (Table 3 and fig. 15B).

The development of stresses within compacted expansive soils due to thermal loading may be considered to originate from thermal dilation, due to an increase in the temperature, and wetting, due to a redistribution of the water content in response to the applied temperature gradient. A decrease in the relative humidity at sections X1 and X2 and no change in the water content at section X3 within a day of thermal loading (fig. 13) suggest that the hydration effect was insignificant, whereas the thermal dilation effect caused an increase in the axial stress closer to the heat source that was transmitted toward the top of the sample (fig. 15A). The radial stress at section X1 was also found to increase due to the thermal dilation phenomenon. This stress may be considered to stem from the net effect of the thermal dilation of the sample and the thermal expansion of the sample ring S3. The thermal expansion of the sample ring S3 was manifested on reduction in the lateral stresses at sections X2 and X3 because the thermal dilation at these sections was less pronounced.

Beyond 1 day from the commencement of thermal loading, the reductions in the axial stress at all levels (fig. 14A and Table 3) were primarily due to a decrease in the sample volume closer to the heat source on account of shrinkage of the sample around section X1, as indicated by a decrease in the water content and the lateral stress at section X1 (figs. 12B, 13B, 14B, and 15B). The lateral stress decrease at section X1 was manifested in an increase in the lateral stresses at sections X2 and X3 (figs. 14B and 15B). The test results showed that thermal loading caused unequal increase in the axial stress and lateral stresses at high- and low-temperature regions (fig. 15). The stress increase was found to be higher toward the low-temperature regions.

Conclusions

The paper presents a newly designed column-type experimental setup for investigating the coupled thermo-hydro-mechanical processes in expansive soils. The sensors and monitoring instruments used provided continuous and nondestructive measurements of key state variables, such as the temperature, water content, relative humidity, and total stress in both axial and lateral directions at various preselected locations. In the context of underground storage of nuclear waste, a compacted sample of bentonite–sand mixture (50:50) was tested under an applied thermal gradient involving 80°C at the bottom and 20°C at the top of the sample. The following conclusions were drawn from the study:

1. The measuring system compliance tests provided information concerning the functionalities and sensitivities of various components within the device. New testing procedures were adopted for studying the response of load cells (axial and radial load cells) and expansion of the PVDF sample cell under elevated mechanical pressure and temperature. The effect of an elevated temperature (80°C) on the thermal expansion of the PVDF sample cell used was found to be insignificant.
2. An application of thermal loading caused changes in the water content and relative humidity within the sample. Temperature equilibration occurred within about 1 day from the commencement of thermal loading. Similar results have been reported in the literature. During the temperature equilibration period, both the water content and relative humidity in the sample closer to the heat source decreased, whereas with an increase in the distance from the heat source, two distinct changes in these parameters were noted, such as

- (1) a combination of an increase in the water content and a decrease in the relative humidity suggested a dominance of thermal dilation in the high-temperature regions of the sample, and (2) a combination of an increase in the relative humidity with no change in the water content suggested that condensation of water vapor may not take place in the cooler regions of the sample if the water vapor is released at the opposite end of the heat source. Beyond 1 day from the commencement of thermal loading, both the relative humidity and water content in the sample increased toward the opposite end of the heat source.
3. Thermal loading caused development of axial and lateral stresses within the sample, the magnitudes of which were different during the short-duration temperature equilibration period (i.e., 1 day) and in longer durations. The impact of thermal dilation at regions closer to the heat source was found to be the key phenomenon contributing to both axial and lateral stress development in the sample during the temperature equilibration period. The lateral stress closer to the heat source decreased due to shrinkage of the sample with an increase in the duration of thermal loading, which, in turn, caused a decrease in the axial stress at both ends of the sample and an increase in the lateral stress in the cooler regions. The lateral stress was found to be greater than the axial stress in the cooler regions of the sample.

ACKNOWLEDGMENTS

The presented study has been performed within the framework of the project “Transient water transport in expansive soils under coupled hydraulic, mechanical and thermal boundary conditions: Experimental and numerical study” funded by Deutsche Forschungsgemeinschaft (DFG), project no. SCHA 675/17-1. The authors are grateful to DFG for the financial support.

References

- Åkesson, M., A. C. Jacinto, C. Gatabin, M. Sanchez, and A. Ledesma. 2009. “Bentonite THM Behavior at High Temperatures: Experimental and Numerical Analysis.” *Géotechnique* 59, no. 4 (May): 307–318. <https://doi.org/10.1680/geot.2009.59.4.307>
- Alonso, E. E., J. Alcoverro, F. Coste, L. Malinsky, V. Merrien-Soukatchoff, I. Kadiri, T. Nowak, H. Shao, et al. 2005. “The FEBEX Benchmark Test: Case Definition and Comparison of Modelling Approaches.” *International Journal of Rock Mechanics and Mining Sciences* 42, nos. 5–6 (July–September): 611–638. <https://doi.org/10.1016/j.ijrmms.2005.03.004>
- ASTM International. 2020. *Standard Practice for Maintaining Constant Relative Humidity by Means of Aqueous Solutions*. ASTM E104-20a. West Conshohocken, PA: ASTM International, approved November 1, 2020. <https://doi.org/10.1520/E104-20A>
- Avallone, E. and T. Baumeister. 2017. *Mark's Standard Handbook for Mechanical Engineers*. New York: McGraw-Hill.
- Börgesson, L., M. Chijimatsu, T. Fujita, T. S. Nguyen, J. Rutqvist, and L. Jing. 2001. “Thermo-Hydro-mechanical Characterization of a Bentonite-Based Buffer Material by Laboratory Tests and Numerical Back Analyses.” *International Journal of Rock Mechanics and Mining Sciences* 38, no. 1 (January): 95–104. [https://doi.org/10.1016/S1365-1609\(00\)00067-8](https://doi.org/10.1016/S1365-1609(00)00067-8)
- Cuevas, J., M. V. Villar, A. M. Fernández, P. Gómez, and P. L. Martín. 1997. “Pore Waters Extracted from Compacted Bentonite Subjected to Simultaneous Heating and Hydration.” *Applied Geochemistry* 12, no. 4 (July): 473–481. [https://doi.org/10.1016/S0883-2927\(97\)00024-3](https://doi.org/10.1016/S0883-2927(97)00024-3)
- Fredlund, D. G., H. Rahardjo, and M. D. Fredlund. 2012. *Unsaturated Soil Mechanics in Engineering Practice*. Hoboken, NJ: John Wiley & Sons.
- Gatabin, C. and P. Billaud. 2005. *Bentonite THM Mock-Up Experiments: Sensors Data Report, Technical Report, Rapport NT-DPC/SCCME 05-300-A*. Paris: Commissariat à l'énergie atomique et aux énergies alternatives (CEA).
- Gens, A., J. Vaunat, B. Garitte, and Y. Wileveau. 2007. “In Situ Behavior of a Stiff Layered Clay Subject to Thermal Loading: Observations and Interpretation.” *Géotechnique* 57, no. 2 (March): 207–228. <https://doi.org/10.1680/geot.2007.57.2.207>
- Martín, P. L. and J. M. Barcala. 2005. “Large Scale Buffer Material Test: Mock-Up Experiment at CIEMAT.” *Engineering Geology* 81, no. 3 (November): 298–316. <https://doi.org/10.1016/j.enggeo.2005.06.013>
- Pintado, X., A. Ledesma, and A. Lloret. 2002. “Back Analysis of Thermohydraulic Bentonite Properties from Laboratory Tests.” *Engineering Geology* 64, nos. 2–3 (May): 91–115. [https://doi.org/10.1016/S0013-7952\(01\)00110-7](https://doi.org/10.1016/S0013-7952(01)00110-7)
- Pusch, R. and R. N. Yong. 2006. *Microstructure of Smectite Clays and Engineering Performance*. London: CRC Press.
- Rawat, A. “Coupled Hydro-mechanical Behavior of a Compacted Bentonite-Sand Mixture: Experimental and Numerical Investigations.” PhD diss., Ruhr-University Bochum, 2019.
- Saba, S., Y. Cui, A. M. Tang, and J. Barnichon. 2014. “Investigation of the Swelling Behaviour of Compacted Bentonite-Sand Mixture by Mock-Up Tests.” *Canadian Geotechnical Journal* 51, no. 12 (April): 1399–1412. <https://doi.org/10.1139/cgj-2013-0377>
- Sellin, P. and O. X. Leupin. 2013. “The Use of Clay as an Engineered Barrier in Radioactive-Waste Management A Review.” *Clays and Clay Minerals* 61, no. 6 (December): 477–498. <https://doi.org/10.1346/CCMN.2013.0610601>

- Schanz, T., W. Baille, and L. Nguyen-Tuan. 2011. "Effects of Temperature on Measurements of Soil Water Content with Time Domain Reflectometry." *Geotechnical Testing Journal* 34, no. 1 (January): 1–8. <https://doi.org/10.1520/GTJ103152>
- Schanz, T., L. Nguyen-Tuan, and M. Datcheva. 2013. "A Column Experiment to Study the Thermo-Hydro-Mechanical Behavior of Expansive Soils." *Rock Mechanics and Rock Engineering* 46, no. 6 (January): 1287–1301. <https://doi.org/10.1007/s00603-012-0361-8>
- Subba Rao, K. S. and S. Tripathy. 2003. "Effect of Aging on Swelling and Swell–Shrink Behaviour of a Compacted Expansive Soil." *Geotechnical Testing Journal* 26, no. 1 (March): 36–46. <https://doi.org/10.1520/GTJ11100J>
- Topp, G. C., J. L. Davis, and A. P. Annan. 1980. "Electromagnetic Determination of Soil Water Content: Measurements in Coaxial Transmission Lines." *Water Resources Research* 16, no. 3 (June): 574–582. <https://doi.org/10.1029/WR016i003p00574>
- Tripathy, S., H. R. Thomas, and P. Stratos. 2017. "Response of Compacted Bentonites to Thermal and Thermo-Hydraulic Loadings at High Temperatures." *Geosciences* 7, no. 3 (July): 53. <https://doi.org/10.3390/geosciences7030053>
- Tripathy, S., H. R. Thomas, and R. Bag. 2015. "Geoenvironmental Application of Bentonites in Underground Disposal of Nuclear Waste: Characterization and Laboratory Tests." *Journal of Hazardous, Toxic, and Radioactive Waste* 21, no. 1 (February): 1–12. [https://doi.org/10.1061/\(ASCE\)HZ.2153-5515.0000272](https://doi.org/10.1061/(ASCE)HZ.2153-5515.0000272)
- Tripathy, S., R. Bag, and H. R. Thomas. 2014. "Effects of Post-compaction Residual Lateral Stress and Electrolyte Concentration on Swelling Pressures of a Compacted Bentonite." *Geotechnical and Geological Engineering* 32, no. 4 (August): 749–763. <https://doi.org/10.1007/s10706-014-9754-7>
- Villar, M. V., P. L. Martín, and J. M. Barcala. 2005. "Modification of Physical, Mechanical and Hydraulic Properties of Bentonite by Thermo-Hydraulic Gradients." *Engineering Geology* 81, no. 3 (November): 284–297. <https://doi.org/10.1016/j.enggeo.2005.06.012>
- Yong, R. N., A. M. O. Mohamed, I. Shooshpasha, and C. Onofrei. 1997. "Hydro-thermal Performance of Unsaturated Bentonite-Sand Buffer Material." *Engineering Geology* 47, no. 4 (October): 351–365. [https://doi.org/10.1016/S0013-7952\(96\)00115-9](https://doi.org/10.1016/S0013-7952(96)00115-9)